

JGR Atmospheres

RESEARCH ARTICLE

10.1029/2024JD042394

Key Points:

- A bow echo forms following the merger of a squall line and a supercell, featured by a rear-inflow jet developing between the two systems
- The supercell drives the rear-inflow jet's dynamic acceleration through its mesoscale and the generation of a deep-tropospheric wave
- Negative horizontal vorticity at the leading edge of the squall line's cold pool causes the rear-inflow jet to descend and expand

Correspondence to:

Y. Du,
duyu7@mail.sysu.edu.cn




Citation:

Yang, H., Du, Y., & Sun, J. (2025). The merger of a supercell and squall line in the Great Plains: 2. Formation of a bow echo. *Journal of Geophysical Research: Atmospheres*, 130, e2024JD042394. <https://doi.org/10.1029/2024JD042394>

Received 4 SEP 2024

Accepted 21 APR 2025

The Merger of a Supercell and Squall Line in the Great Plains: 2. Formation of a Bow Echo

Hongpei Yang¹ , Yu Du^{1,2,3} , and Juanzhen Sun⁴ 

¹School of Atmospheric Sciences, Sun Yat-sen University, and Southern Marine Science and Engineering Guangdong Laboratory (Zhuhai), Zhuhai, China, ²Guangdong Province Key Laboratory for Climate Change and Natural Disaster Studies, Sun Yat-sen University, Zhuhai, China, ³Key Laboratory of Tropical Atmosphere-Ocean System, Sun Yat-sen University, Ministry of Education, Zhuhai, China, ⁴National Center for Atmospheric Research, Boulder, CO, USA

Abstract The merger of squall line and supercell has been commonly observed in the Great Plains of the United States. On 23–24 May 2020, an isolated supercell formed ahead of a squall line and subsequently evolved into a bow echo through their merger. Utilizing a 10-min update four-dimensional variational data assimilation system that integrates radar and surface observations, we investigated the convective-scale processes that led to the formation of this bow echo. Our findings indicated that as the squall line advanced eastward, its inflow was initially obstructed by the supercell, causing the weakening of both the squall line and its associated cold pool. However, during the merger, a strong rear inflow jet (RIJ) rapidly developed ahead of the squall line's leading edge and behind the supercell. Unlike a classic RIJ that typically expands rearward over the cold pool, this RIJ accelerated forward toward the supercell. Diagnostic pressure analysis revealed that the RIJ was primarily driven by the developing mesoscale embedded within the supercell. Additionally, the supercell's strengthening prior to bowing generated a deep-tropospheric gravity wave downdraft, which amplified the RIJ by enhancing near-surface westerlies. Despite the weakening of the squall line's cold pool, it still contributed to the RIJ formation by providing negative horizontal vorticity at its leading edge and facilitating the RIJ's descent. Consequently, the intense RIJ and the subsequent replacement of the supercell against the initial leading edge led to the formation of a severe bow echo, producing a broad swath of damaging winds.

Plain Language Summary A classic bow echo typically evolves from a linear convective system and is characterized by a rear-inflow jet (RIJ) above the cold pool. In contrast, many bow echoes in the Great Plains of the United States result from the merger of a squall line and a supercell. Despite their severe weather impact, the detailed mesoscale and convective-scale processes governing the formation of these bow echoes through such mergers remain insufficiently understood. In this study, we identified a previously undocumented RIJ that developed in the gap between a squall line and a supercell before their merger, which played a crucial role in the subsequent development of a bow echo. This RIJ and its forward expansion were mainly resulted from the strong low-level pressure deficit within the rotating supercell. Additionally, a deep-tropospheric wave downdraft originating from the supercell, combined with the negative buoyancy associated with the squall line's cold pool, further contributed to the RIJ's formation. This paper provides a comprehensive analysis into the key processes leading to the formation of a bow echo through the merger from an observational perspective, offering valuable insights for improving its accurate forecast.

1. Introduction

Bow echoes, characterized by their distinctive bow-shaped radar signatures, are a subset of mesoscale convective systems known for producing long-swath of high winds and occasionally tornadoes (Davis et al., 2004; Fujita, 1978; Jirak et al., 2003; Przybylinski, 1995; Wakimoto, Murphey, Davis, & Atkins, 2006; Wakimoto, Murphey, Nester, et al., 2006; Weisman, 1993; Wheatley et al., 2006). First documented by Nolen (1959) and further defined by Fujita (1978), bow echoes have been extensively studied due to their destructive potential and impact on both lives and property.

Bow echoes typically originate from squall lines but are more likely to form in environments with higher convective available potential energy and moderate-to-strong ($15\text{--}20\text{ m s}^{-1}$) low-level shear (e.g., Trapp & Weisman, 2003; Weisman, 1992, 1993; Weisman & Davis, 1998; Weisman & Trapp, 2003). Their formation has been consistently linked to the presence of a strong rear inflow jet (RIJ; e.g., Atkins et al., 2004; Forbes &

Wakimoto, 1983; Jorgensen & Smull, 1993; Przybylinski, 1995). The RIJ accelerates the convective cells at the center of the system, thereby creating the distinctive bow shape (Smull & Houze, 1987; Weisman, 1992, 2001). The development of the RIJ follows the strengthening of the convectively generated cold pool over time. The RIJ initially accelerates in response to the mid-level mesolow hydrostatically generated by the vertical buoyancy gradient behind the convective updraft (Lafore & Moncrieff, 1989; Smull & Houze, 1987). Over time, the RIJ strengthens further and expands rearward due to the horizontal buoyancy gradients along the cold pool's trailing edge (Weisman, 1992, 1993). The counter-rotating bookend vortices at the ends of the bowing segment can also enhance the RIJ and contribute to its bowing (Grim et al., 2009; Weisman, 1993; Weisman & Davis, 1998). Occasionally, the RIJ at the bow apex descends to the surface as a downdraft, producing damaging winds when the cold pool circulation overwhelms environmental shear (Fujita, 1978, 1979; Weisman, 1992).

Beyond squall lines, a notable proportion of bow echoes originate from other convective structures, such as weakly organized cells or supercells (Finley et al., 2001; Goodman & Knupp, 1993; Klimowski et al., 2004; Moller et al., 1994; Zhou et al., 2023). Climatology studies suggest that about half of bow echoes in the United States result from thunderstorm mergers (Burke & Schultz, 2004; Klimowski et al., 2004). French and Parker (2012) analyzed squall line-supercell mergers and found that they consistently evolve into bow echoes, with a shift in severe weather from hail before the merger to severe winds and tornadoes after bowing, in agreement with earlier case studies (Fujita, 1978; Sieveking & Przybylinski, 2004). However, the specific physical processes governing bow echo formation during mergers have received limited attention. Idealized simulations (French & Parker, 2014, hereafter FP14) have revealed that such mergers can promote more compact bow echoes due to enhanced cold pools and RIJs. Specifically, as the squall line encounters the supercell, the cold pools of the two systems merge and deepen. Additionally, the supercell's mesocyclone intensifies the cyclonic bookend vortex, strengthening RIJ. These idealized simulations showed similarities to the general evolution of real mergers but the verification of the simulated storm-scale processes has not been performed due to limited observational data (e.g., radar network). Consequently, the applicability of these conclusions and the variability of processes across different scenarios remain uncertain.

Recently, a canonical merger event took place over the Great Plains on May 23–24, 2020. As envisioned in FP14, a large bow echo emerged as the squall line overtook the isolated supercell ahead of it. Developed in a relatively weak synoptic environment (refer to Part 1; Yang et al., 2025), we believe that storm-scale processes are more essential. The main goal of this study is therefore to comprehensively investigate the key processes in the genesis of this bow echo from an observational perspective, with comparisons against idealized merger simulations (FP14) and the classical bow echo (e.g., Weisman, 1993). Our preliminary examination of the high resolution ensemble forecast shows deviations in the morphology of the squall line, as well as variations in the location and timing of the supercell and the resulting bow echo (not shown). In this context, we opted for the four-dimensional variational data assimilation system (VDRAS) to examine the evolution of this merger event. VDRAS has been shown to excel in severe weather analyses and forecasts worldwide (see Sun et al., 2023 for a review). Using Weather Research and Forecasting (WRF) model outputs as the initial guess background, VDRAS assimilates Doppler radars and surface observations to retrieve three-dimensional thermodynamic and dynamic fields, ensuring a more reliable analysis closer to reality (Chen et al., 2016; Zhang et al., 2021). The configuration and verification of VDRAS are detailed in Part 1 (Yang et al., 2025), where we demonstrated that VDRAS analysis significantly improves accuracy compared to the WRF first-guess input during this merger event. The VDRAS domain is shown in Figure 1.

The remainder of the paper is laid out as follows. Section 2 describes the evolution of the observed squall line–supercell merger in the Great Plains and discusses the associated severe weather reports, followed by a comparison of two contrasting RIJs occurring before and during the merger. Section 3 evaluates the key processes leading to the acceleration of the RIJ during the merger, which ultimately forms the bow echo. The roles of the supercell, the squall line's cold pool, and the bookend vortices are illustrated in this section. Finally, we summarize our findings, and compare similarities and differences with previous studies in Section 4.

2. Evolution of Bow Echo and RIJs

2.1. Squall Line–Supercell Merger and the Formation of Bow Echo

The merger of the squall line and supercell occurred at night (LST = UTC-5) in the central Great Plains of the U. S. As shown in Figure 2, an isolated supercell initiated ahead of the squall line and mainly developed in situ (the

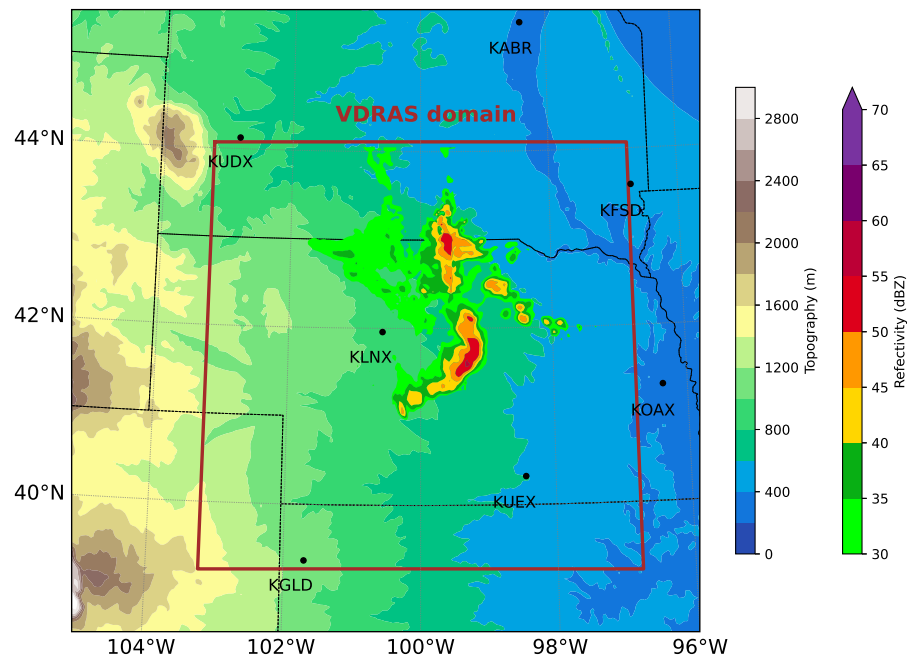


Figure 1. Domain configuration of VDRAS and the column maximum radar reflectivity (dBZ) at 0100 LST showing the bow echo on 24 May 2020. The locations of the seven NEXRAD radars used in VDRAS are marked with text labels.

initiation mechanisms have been discussed in Part 1; Yang et al., 2025). The squall line propagated eastward at a speed of approximately 11 m s^{-1} as determined by the movement of 30 dBZ reflectivity before 0000 LST. During its propagation, a strong RIJ exceeding 18 m s^{-1} at 1.35 km above ground level (AGL) was observed on the northern side of the squall line (Figure 2c). However, this RIJ didn't produce a bow echo and soon weakened (Figures 2a–2d). Note that the speed of RIJ was storm-relative, that is, it was obtained by subtracting the propagation speed of the squall line.

The merging process started as the squall line shifted further eastward. Similar to the idealized simulation results by FP14, the squall line initially exhibited a weakening in its southern segment (Figures 2d and 2e), primarily due to the blocking of inflow by the supercell ahead (Figures 3a and 3b). Prior to bowing, a new RIJ formed on the southern side of the squall line, behind the supercell. This RIJ also reached an intensity of 14 m s^{-1} and persisted for more than 1 hour (Figures 2f–2h), possibly contributing to the formation of the bow echo. Meanwhile, the original leading edge shifted farther east as the outflow from the squall line converges strongly with the supercell inflow, with the supercell's blocking effect cutting off the squall line's inflow. A compact and large bow echo emerged after 0030 LST as the merged system adopted the supercell's leading edge (Figure 3c). The bow segment was most prominent at 0100 LST (Figure 2g).

The evolution of the reflectivity swath for this event and the associated severe weather reports from SPC (storm prediction center) are shown in Figure 4. Both the squall line and the supercell produced hail, but the hail reports were more closely linked to the supercell before the merger. In contrast to hail, damaging winds were generated over a broad region, mostly (12 out of 16 reports) after the merger while no events were recorded during the merger, indicating that they were the product of the bow echo as the RIJ descended to the ground. The most damaging derecho recorded was approximately 35.7 m s^{-1} at 0115 LST when the bow segment was notable. However, even when the bow segment was less evident, severe winds exceeding 30 m s^{-1} were still observed over a broad area (Figures 2i and 4).

2.2. Development of Two RIJs Before and During the Merger

In contrast to previous studies on bow echoes formed by mergers, two RIJs with different locations relative to the squall line are found to form before and during the merger. Before the merger, rear inflow developed intensively behind the northern squall line, becoming an RIJ at approximately 2230 LST (Figures 2a and 2b). Half an hour

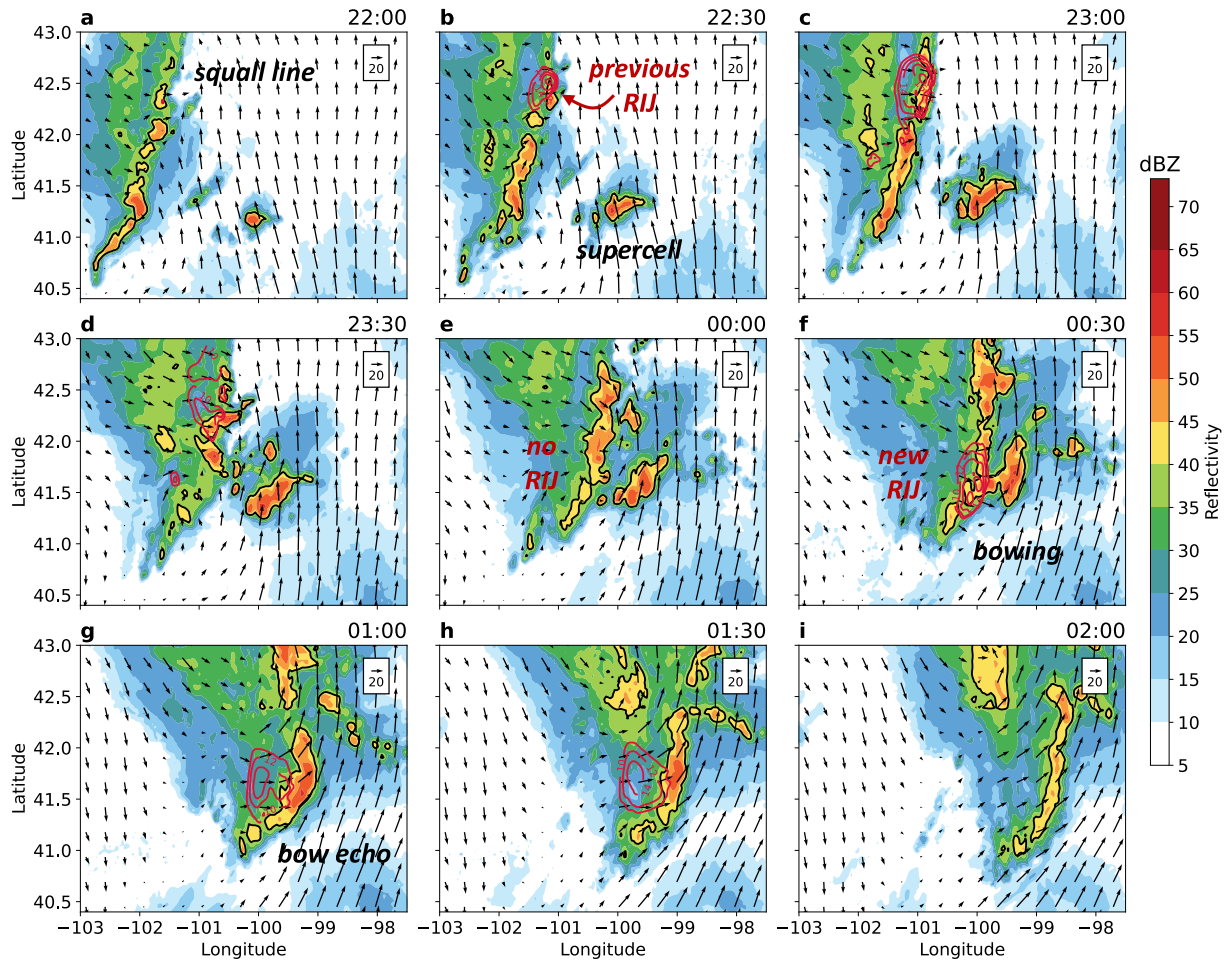


Figure 2. Observed column maximum reflectivity (shading, dBZ; black contour, 40 dBZ) and VDRAS wind vectors for the squall line-supercell merger at (a) 2200, (b) 2230, (c) 2300, (d) 2330, (e) 0000, (f) 0030, (g) 0100, (h) 0130, and (i) 0200 LST on 23–24 May 2020 in the Great Plains. Squall line-relative zonal winds at 1.35 km above ground level (starting from 10 m s^{-1} at an interval of 2 m s^{-1}), representing RIJs, are contoured in red.

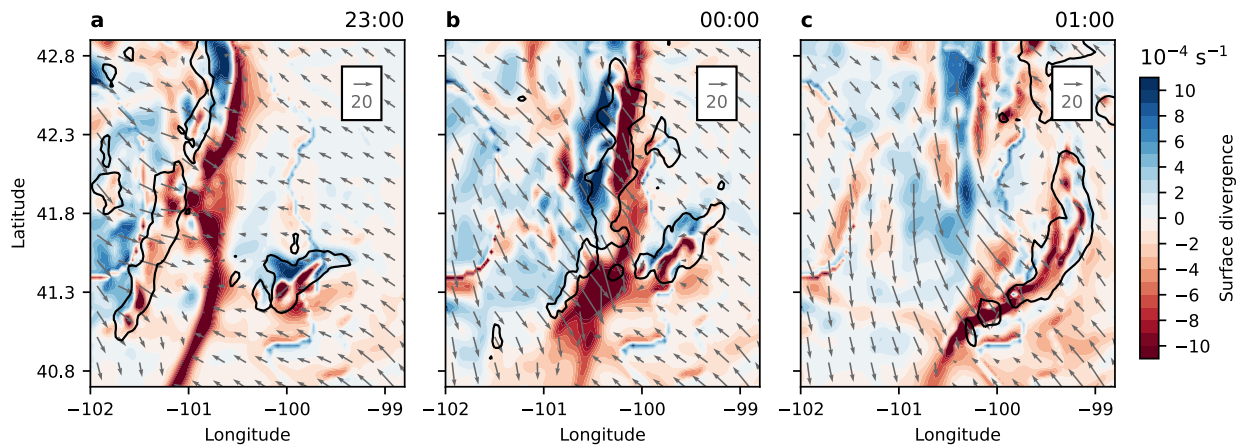


Figure 3. Distribution of VDRAS surface divergence and wind vectors at (a) 2300, (b) 0000, and (c) 0100 LST. The composite radar reflectivity of 40 dBZ is delineated by black contours.

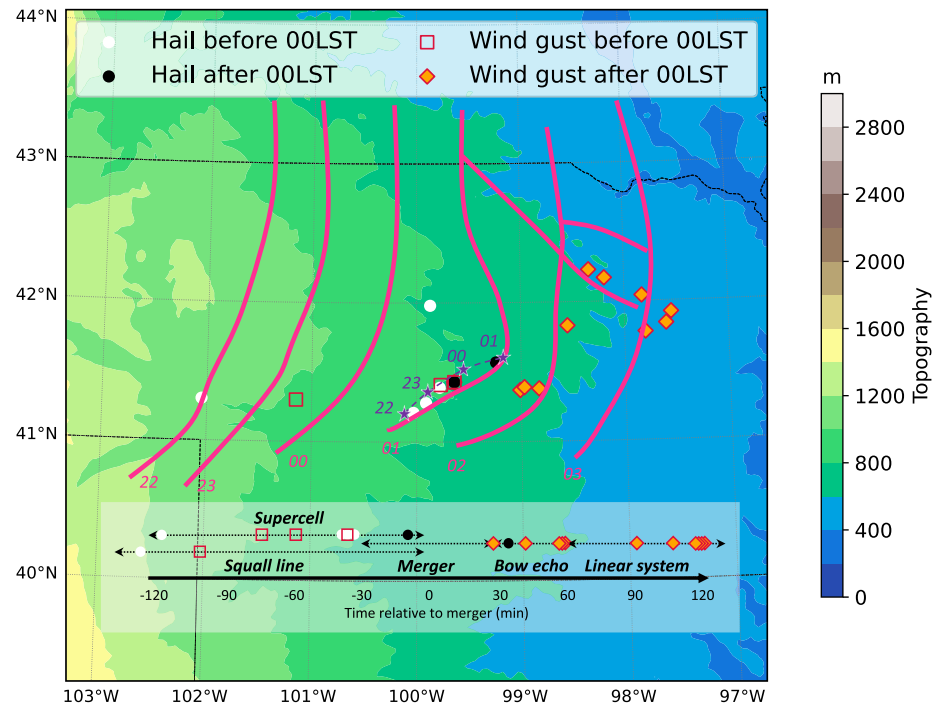


Figure 4. Evolution of the bow echo resulting from the squall line-supercell merger, along with associated hail (dots) and wind gust (squares and diamonds) events between 2200 and 0300 LST on 23–24 May 2020. Pink lines delineate the approximate locations of 35 dBZ reflectivity swaths, while purple line and stars show the migration of the supercell before 0100 LST. The shaded area represents the topography (m) within the VDRAS domain. The timeline at the bottom illustrates the event progression, highlighting the timing of severe weather reports relative to the merger ($t = 0$, 0030 LST).

later, this northern RIJ reaches its maximum intensity of 18 m s^{-1} and then gradually weakens to below 8 m s^{-1} (Figure 2e) due to the weakening of the squall line, as indicated by the broken convective echoes (Figure 2d).

The formation of this RIJ is closely related to the convectively generated cold pool. As shown in Figure 5, a prominent midlevel pressure minimum is found above the cold pool, approximately parallel to the cold pool gust front (as defined by the -2 K perturbation surface temperature, Figure 5a). To find out what contributed to this pressure minimum, a diagnosis of the mid-level pressure deficit p' is performed through the pressure equation (Klemp, 1987):

$$-p' \propto \nabla^2 p' = \underbrace{\frac{\partial B}{\partial z}}_{p'_b} - \underbrace{\nabla \cdot [(\bar{\rho} \vec{V} \cdot \nabla) \vec{V}]}_{p'_d} + \text{res} \quad (1)$$

where \vec{V} is the 3D wind vector, $\bar{\rho}$ is the air density and B is the buoyancy. On the right-hand side of Equation 1, the first term is commonly known as the buoyancy term p'_b , primarily accounting for hydrostatic effects. The second term on the right-hand side, is often referred to as dynamic pressure perturbation p'_d as it is attributed to the variations in velocity. The residual term includes processes such as the Coriolis force and β effect, which should be small on the convective scale. In this study, p'_d was calculated by subtracting p'_b from $\nabla^2 p'$. The vertical cross-section of the pressure field normal to the gust front shows that the low pressure is mainly associated with the minimized p'_b (green contours in Figure 5b) above the deep cold pool ($>2 \text{ km}$). The RIJ increases and expands rearward in response to the developing midlevel mesolow. Hence, this RIJ, which is highly consistent with the classic theory, is a direct result of the upshear-tilting updraft rearward of the squall line cold pool (Smull & Houze, 1987; Weisman, 1993), rather than the merger process.

As the squall line propagates further eastward, its inflow is cut off by the rotating supercell. A notable weakening of the gust front convergence is shown in the central squall line (Figure 3b). Meanwhile, the near-surface flow

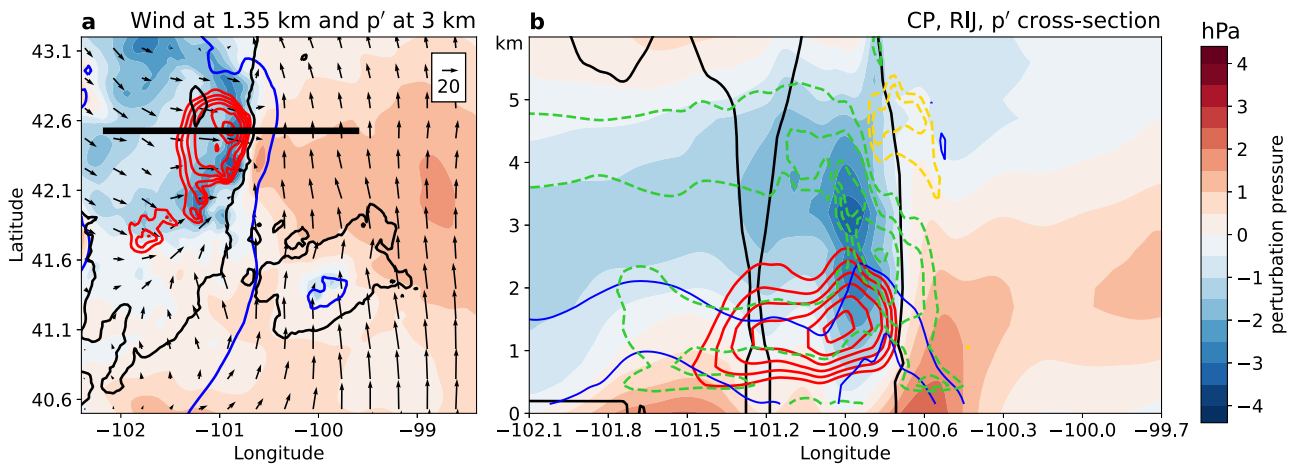


Figure 5. Pressure perturbations associated with squall line-supercell merger at 2300 LST on 23 May 2020. (a) Horizontal distribution of perturbation pressure (shading, hPa), relative to the field at 2000 LST, at 3 km above ground level (AGL) with wind vectors, squall line-relative zonal winds (red contours, starting from 8 m s^{-1} at an interval of 2 m s^{-1}) at 1.35 km AGL, the cold pool (blue contour, -2 K at the lowest VDRAS level) and the composite radar reflectivity (black contour, 20 dBZ). (b) Vertical cross-section of perturbation pressure (shading, hPa), squall line-relative zonal winds (red contours of 8, 10, 12, 14 m s^{-1}), diagnosed buoyancy (green contours of $-9, -6, -3 \times 10^{-3} \text{ Pa m}^{-2}$), and dynamic pressure perturbation (yellow contours of $-9, -6, -3 \times 10^{-3} \text{ Pa m}^{-2}$), along the black line in (a). Blue contours ($-2, -4 \text{ K}$ temperature perturbation) indicate the squall line cold pool, and the black contour (25 dBZ radar reflectivity) shows the squall line.

also shifts from easterlies to northerlies, enhancing convergence in the south. Consequently, the magnitude of the northern RIJ decreases as the squall line weakens (Figures 2d and 2e).

However, a new RIJ, albeit relatively weaker ($\sim 14 \text{ m s}^{-1}$) than the previous classic RIJ, established during the merger and subsequently contributed to the formation of the bow echo. It is located in the southern portion of the squall line and right behind the supercell, indicating its role during the merger. In contrast to the northern RIJ, this merger-resulting RIJ also differs in its relative location to the cold pool. It is first observed ahead of the squall line cold pool, where the near-surface cold air is shallow (Figure 6b and cf. Figure 5b). Even during the merger, it persistently develops in the gap between the squall line cold pool and the supercell, suggesting a much more complex governing mechanism in its formation. In the following section, we will detail how the supercell and the squall line contribute to its establishment and the resulting bow echo.

3. Formation of RIJ During the Merger

3.1. Role of Supercell Mesolow and Gravity Wave

Since the new RIJ is generated in response to the merging process, its evolution in association with the supercell is presented in Figure 6. Although a notable midlevel low-pressure center is found above the squall line cold pool, it exhibits a decreasing trend due to the weakening and shallowing of the cold pool (Figure 6). Instead, the RIJ is observed to accelerate ahead of the cold pool and behind the supercell, where the most significant decrease in pressure is shown. This enhancement of low pressure is linked to the development of the supercell. As shown in Figure 6, low pressure develops extensively near the supercell, extending from the surface to above 3 km AGL, with a mesolow centered inside the supercell. As we have discussed in Part 1 (Yang et al., 2025), the generation of the mesolow was supported by the high shear inflow ($>20 \text{ m s}^{-1}$ in the lowest 3 km), which favors the rotation of updraft by the tilting of horizontal vorticity (Rotunno & Klemp, 1985; Wilhelmson & Klemp, 1978).

Diagnostic pressure analysis shows that both the buoyancy and dynamic terms contribute significantly to the formation of the mesolow. The buoyancy-driven pressure perturbation p'_b acts mainly below 1 km AGL because the supercell-generated cold pool is relatively weak. The relatively low altitude of p'_b may also aid in the descent of the RIJ during its evolution (Figure 6d). However, p'_d , located at a higher altitude between 1 and 2 km AGL where the RIJ also maximized, demonstrates its important role in RIJ formation. Indeed, this is quite common for supercells, as the persistent rotating updraft (or mesocyclone, usually at mid-levels) dynamically produces strong perturbation pressure gradients (e.g., Klemp, 1987). Moreover, classic RIJs typically expand rearward of the squall line cold pool (e.g., Figures 2b and 2c) due to the strong rearward pressure gradient generated by p'_b (e.g.,

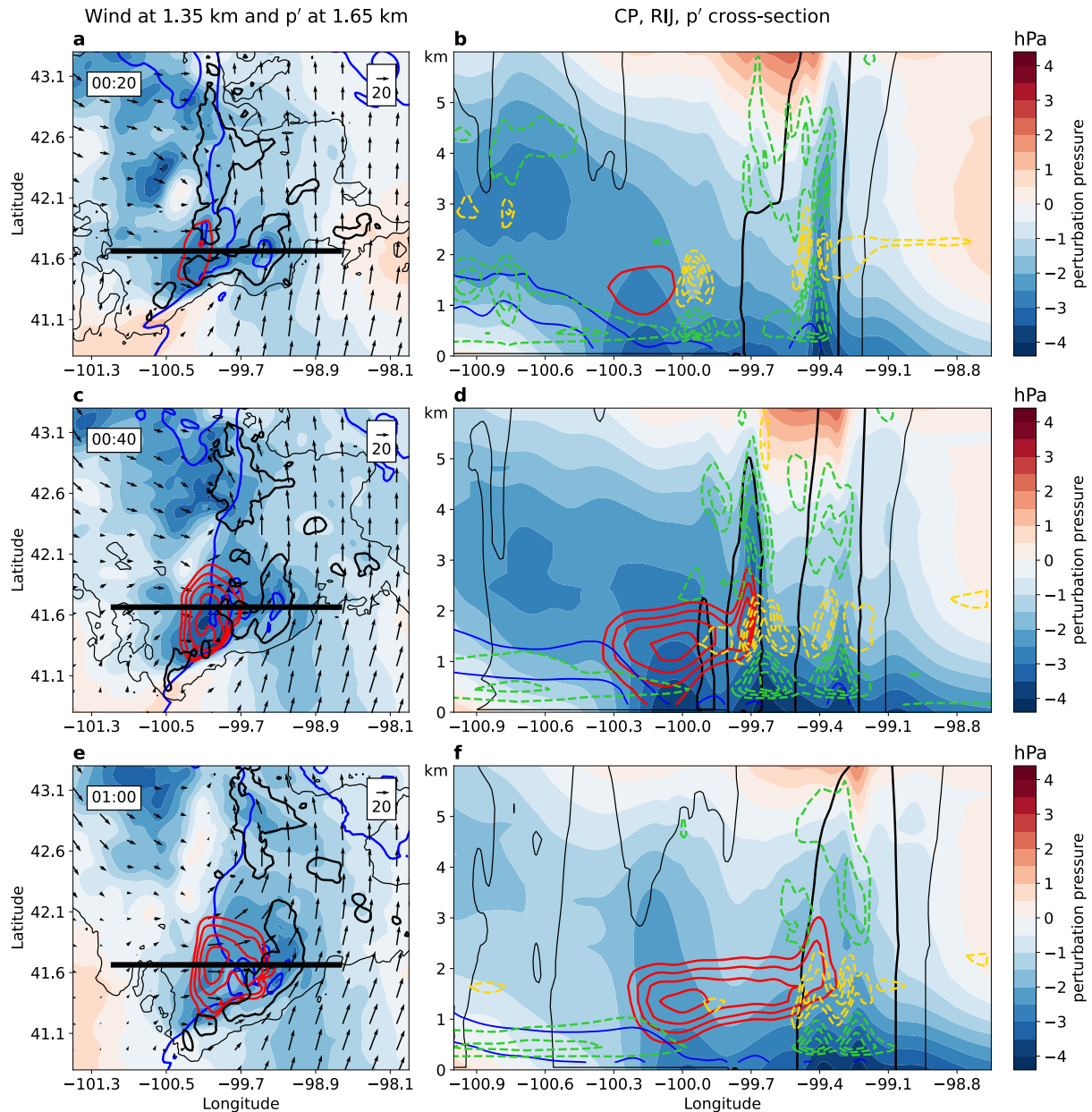


Figure 6. As in Figure 5, but at (a, b) 0020, (c, d) 0040, (e, f) 0100 LST. Black thick and thin contours represent radar reflectivity at the levels of 40 and 20 dBZ, respectively.

Figure 5b). Although initially established above the squall line cold pool, this RIJ later exhibits a forward expansion toward the supercell, as clearly shown by the range of red contours in Figures 5f–5h and 6. This finding further indicates that, in such a scenario, the supercell mesolow dynamically accelerates the RIJ forward by producing a pressure gradient ahead of the squall line cold pool.

This rear-to-front acceleration can also be partially explained through wave dynamics (Xu et al., 2024; Yang & Du, 2024). As shown in Figure 7a, the system-relative streamline field initially displays weak inflow and updraft near the tip of the squall line's leading edge. Simultaneously, a prominent downdraft forms near the supercell (Figure 7a) and gradually propagates westward (Figure 7c). The time-height diagram of wind at 100°W illustrates that the downward motion peaks at approximately 5–7 km AGL, corresponding to an $n = 1$ wave (Du et al., 2024; Nicholls et al., 1991). In addition, concurrent changes in wind and pressure fields (in-phase $p' - u'$) in the lower-

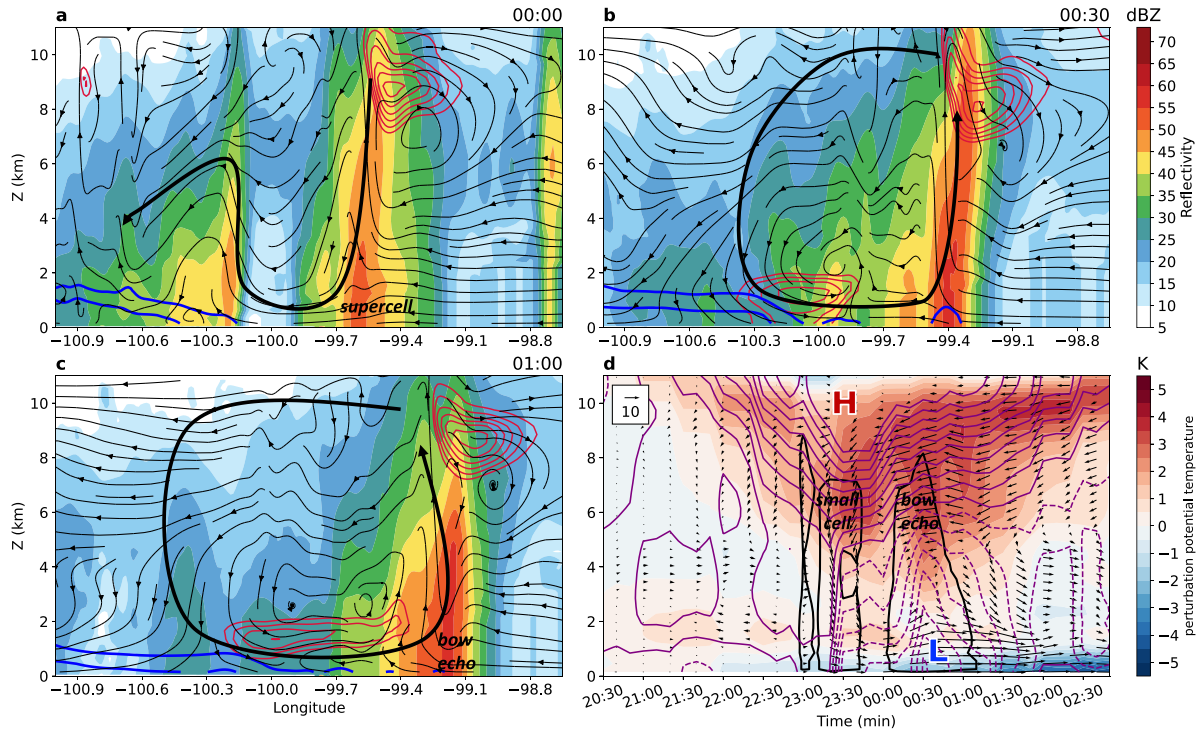


Figure 7. Vertical cross-sections of radar reflectivity (shading, dBZ), system-relative convective flows (streamlines) and meridional winds (red contours, starting from 8 m s^{-1} at an interval of 2 m s^{-1}) along the black line in Figure 6 at (a) 0000, (b) 0030, and (c) 0100 LST on 24 May 2020. Blue contours (-2 , -4 K temperature perturbation) in (a–c) indicate the cold pool. The wave-like circulation generated is marked by black curved arrows. (d) Time-height diagram of the perturbation potential temperature (shading, K), perturbation pressure (purple contours, K), wind vectors (u' and 10-times w , m s^{-1}), radar reflectivity (black contour, 25 dBZ) and radar reflectivity (black contour, 25 dBZ) at (100°W , 41.65°N).

troposphere, well resolved in VDRAS, indicate the presence of a wave (Figure 7d). For waves generated by deep convection, the vertical structure of vertical motion \hat{w} is closely linked to variations in the heating profile,

$$\hat{w}_n(z) = \frac{Q_0 \sin(m_n z)}{N^2}$$

where Q_0 is the heating amplitude, $m_n = n\pi/H$ is the vertical wavenumber for trapped waves of n -th mode between the surface ($z = 0$) and the tropopause ($z = H$), and N is the Brunt–Väisälä frequency. The heating amplitude is given by $Q_0 = g/\theta_0(\partial\theta'/\partial t)$, where g is the gravitational acceleration, θ' and θ_0 are perturbation and background potential temperature, respectively. An $n = 1$ wave is typically triggered by enhanced heating throughout the troposphere, often due to increased latent heat release from convective updrafts. As shown in Figure 8a, the supercell's updraft intensifies significantly prior to merging, resulting in a steady increase in virtual potential temperature (Figure 8b), favoring wave generation. Taking $\partial\theta'/\partial t = 0.002 \text{ K s}^{-1}$ (Figure 8b) and a mean N of 0.01 s^{-1} within troposphere (not shown), the estimated vertical structure for $\hat{w}_{n=1}$ aligns well with the observed w profile (Figure 8c).

As the wave downdraft propagates horizontally through the atmosphere, it significantly inhibits convective development along the squall line's gust front (Figures 7c and 7d). The wave is characterized by a noticeable enhancement of near-surface westerlies and high-level easterlies, which lag the arrival of the downdraft and contribute to the formation of the RIJ between the squall line and supercell (Figures 7a–7c). Similarly, we can estimate the wave-induced horizontal velocity (\hat{u}) using the continuity equation:

$$\hat{u}_n(z) = i(\partial\hat{w}_n/\partial z)/k,$$

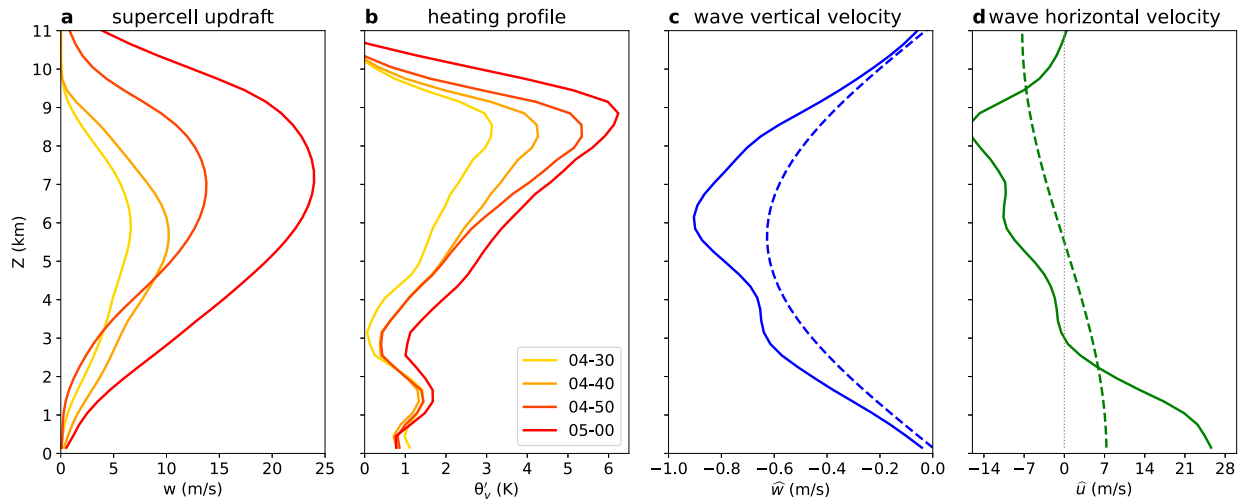


Figure 8. Vertical profiles of (a) vertical motions (m s^{-1}) and (b) maximum perturbation virtual potential temperature (K) within the supercell at different times. Vertical profiles of (c) vertical motion at (100°W , 41.65°N) at 2340 LST (blue solid line) and estimated wave vertical velocity (blue dashed line), and (d) horizontal motion at (100°W , 41.65°N) at 0040 LST (green solid line) and estimated wave horizontal velocity (green dashed line).

where k is horizontal wavenumber. Figure 7 illustrates that the variation in pressure p' lags the vertical motion w by approximately 30 min, indicating a frequency $\omega = 2\pi/120 \text{ min} = 8.7 \times 10^{-4} \text{ s}^{-1}$. Applying the dispersion relation (assuming $\omega > 0, k = -m\omega/\sqrt{N^2 - \omega^2}$), we derived the vertical profile of $\hat{u}_{n=1}$, which exhibits the largest westerly flow at the surface ($\hat{u}_{n=1,z=0} = 7.3 \text{ m s}^{-1}$) and an overall contribution of about 20% to the RIJ (Figure 8d).

3.2. Role of Squall Line Cold Pool

The convectively generated cold pool, which typically creates a midlevel pressure minimum and induces rear-to-front accelerations (e.g., the northern classic RIJ), has been widely recognized as one of the primary drivers in many previous studies of RIJs. Additionally, idealized numerical simulations have shown that the initial squall line cold pool strengthens locally, with its depth increasing from ~ 1.5 to ~ 3 km when it merges with a supercell's cold pool, leading to a more pronounced RIJ and the production of a bow echo (FP14). However, in our case, these storm-scale processes associated with the cold pool exhibit unique characteristics during the merger (Figures 5 and 6).

We first examine the horizontal distribution and temporal variation of the cold pool at the lowest level in VDRAS (Figure 9). As shown in Figure 9d, the squall line cold pool and its associated vertical buoyancy gradient initially strengthen prior to the merger, reaching a maximum intensity around 2320 LST. This strengthening greatly contributes to the genesis of the northern classic RIJ during the same period (Figure 5). However, during the merger, the squall line's cold pool instead shows a weakening trend, with its magnitude decreasing by approximately 2 K within 1 hour (Figure 9) and its depth reducing to only ~ 1 km (Figure 6). Consequently, the buoyancy effect of the cold pool becomes minimal after 0000 LST. Although the supercell produces its own cold pool before the merger, it is notably weaker compared to the squall line's cold pool and gradually diminishes. By 0100 LST, the -2 K temperature perturbation contour is scarcely discernible. Consequently, during the merger, the distinct merging of the two cold pools is not evident (Figure 9c). As analyzed in Section 3.1, the weakening cold pool has a secondary impact on RIJ formation.

In addition to the hydrostatic effects induced by the cold pool, its role can be understood from a horizontal vorticity perspective. A cold pool is typically associated with negative buoyancy B , which decreases horizontal vorticity η ahead of it via the two-dimensional horizontal vorticity equation (Weisman, 1992, 1993):

$$\frac{d\eta}{dt} = -\frac{\partial B}{\partial l}, \quad (2)$$

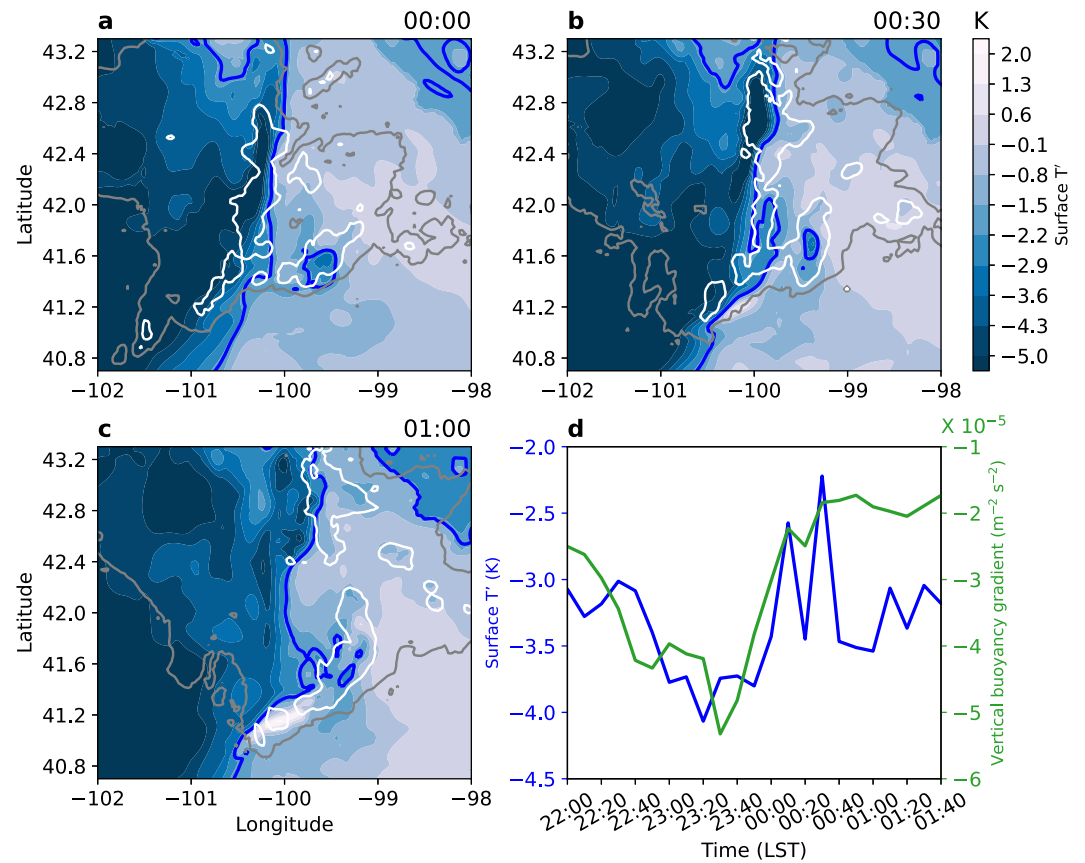


Figure 9. Horizontal distribution of temperature perturbations (shading, K) at the lowest VDRAS level and the composite radar reflectivity (white contour, 40 dBZ; gray contour, 20 dBZ) at (a) 0000, (b) 0030, and (c) 0100 LST on 24 May 2020. Blue contours (-2 K surface temperature perturbation) indicate the cold pool leading edge. (d) Temperature perturbations (blue line) at the lowest VDRAS level and the mean 0–3 km vertical buoyancy gradient $\partial B / \partial z$ (green line) averaged within a 20 km-wide area rearward the leading edge of the squall line's cold pool at 41.65°N.

where $\eta = \frac{\partial u}{\partial z} - \frac{\partial w}{\partial l}$. Here, l represents the scalar unit of the distance along the thick black line in Figure 6 (approximately in the zonal direction) since the squall line's cold pool propagates approximately eastward. The vertical cross-sections along the line perpendicular to the cold pool orientation show that negative horizontal vorticity is most evident within the RIJ region, exceeding $-5 \times 10^{-3} \text{ s}^{-1}$ at 0020 LST and continuing to strengthen throughout the merger (Figure 10). Our focus is on the horizontal vorticity tendency associated with cold pools, which produces a horizontal buoyancy gradient. As expected, positive $\frac{\partial B}{\partial l}$ is evident at the cold pool's leading edge (100°W, Figure 10a), potentially contributing to the initial acceleration of the RIJ. However, the magnitude of $\frac{\partial B}{\partial l}$ at the leading edge decreases significantly as the cold pool weakens, while inside the supercell it becomes stronger, promoting the forward expansion of the RIJ. In this scenario, relatively smaller negative horizontal vorticity near the leading edge (100.1°W in Figure 10b) enhances downward motions locally, thus descending the RIJ toward the ground and constraining its development ahead of it (Figure 10b).

3.3. Role of Bookend Vortices

Another key component influencing the evolution of the bow echo and the system-relative flow at mid-levels (i.e., RIJ) is the development of the bookend vortices, consisting of both cyclonic and anticyclonic vortices (Grim et al., 2009; Weisman, 1993). As suggested by FP14, the merged supercell, which includes a mesocyclone, could potentially enhance the cyclonic vortex, thereby amplifying the RIJ and promoting bow echo formation. Investigating the role of these vortices in this specific case is therefore of particular interest.

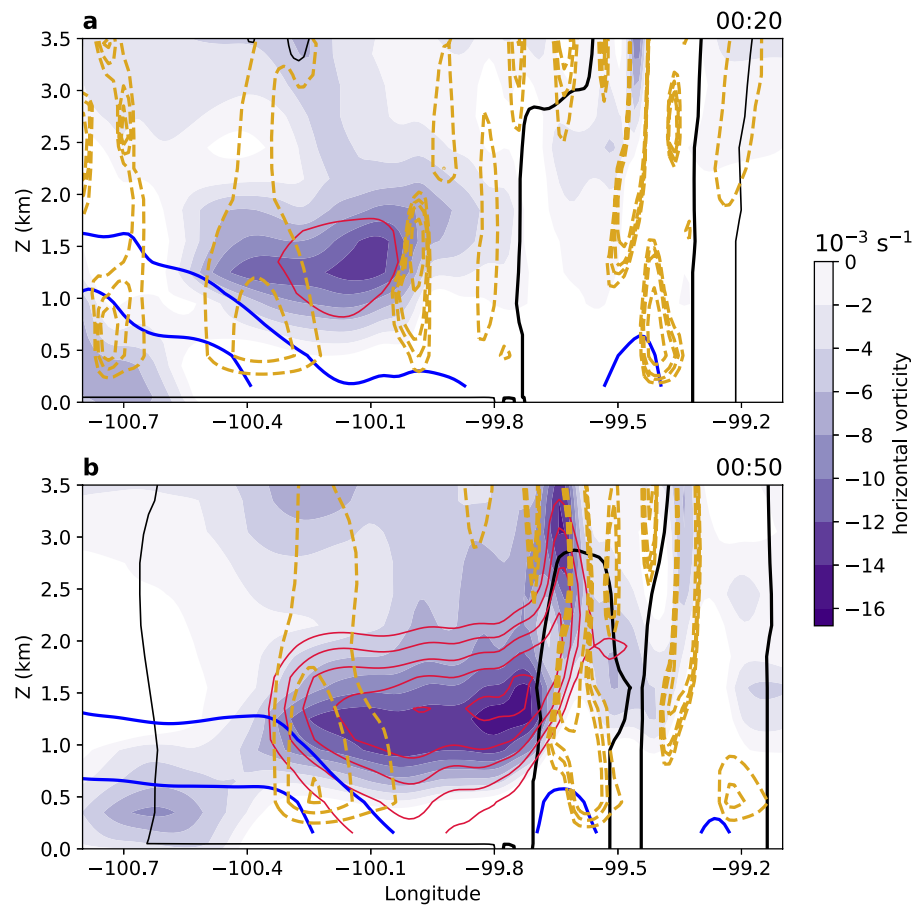


Figure 10. Vertical cross-sections of horizontal vorticity (shading, s^{-1}), the along-line gradient of buoyancy (yellow contours at $2, 4, 6, 8 \times 10^{-6} \text{ s}^{-2}$), system-relative meridional winds (red contours, starting from 8 m s^{-1} at an interval of 2 m s^{-1}), and radar reflectivity (thick black contours for 40 dBZ and thin black contours for 20 dBZ) along the thick black line in Figure 6 at (a) 0020 and (b) 0050 LST. Blue contours ($-4, -2 \text{ K}$ temperature perturbation) indicate the cold pool.

First, we examine the diagnosed vertical vorticity (ζ) field at 1.35 km AGL where the core of the RIJ is located. As shown in Figure 11, a pair of counter-rotating vortices is evident at the north and south ends of the squall line. Alongside these bookend vortices, a distinct mesocyclone is observed within the supercell, mainly persisting in its original location until the formation of the bow echo. At the onset of the merger, the cyclonic vortex exhibits notably greater intensity compared to the relatively weaker anticyclonic vortex (Figure 11a). However, over the subsequent hour, as the squall line approaches the supercell, the cyclonic vortex experiences significant weakening (Figures 11a–11d). This weakening contrasts with findings from previous bow echo studies, where an enhancement of the vortices was often observed (Grim et al., 2009; Wakimoto et al., 2015). In this case, the weakening trend may be linked to the reduced intensity of the squall line cold pool (Figure 9), as the bookend vortices primarily originate from the tilting and subsequent stretching of cold pool-generated horizontal vorticity (Weisman & Davis, 1998). During the merger process, the south anticyclonic vortex shows a slight enhancement around 0030 LST (Figure 11b). Notably, the weakening in the cyclonic vortex far exceeds the intensification of the anticyclonic vortex, demonstrating that while bookend vortices evolve alongside the RIJ, they may not be the primary driving factor behind its acceleration.

To quantitatively assess the contribution of these vortices to the westerly flow accompanying RIJ development, we perform calculations by superimposing the bookend vortices onto the flow using the inverse two-dimensional Poisson Equation 3 for the streamfunction ψ (Wakimoto, Murphey, Davis, & Atkins, 2006; Xu et al., 2015). This assumes zero vertical vorticity (or streamfunction) at the lateral boundaries of the VDRAS domain.

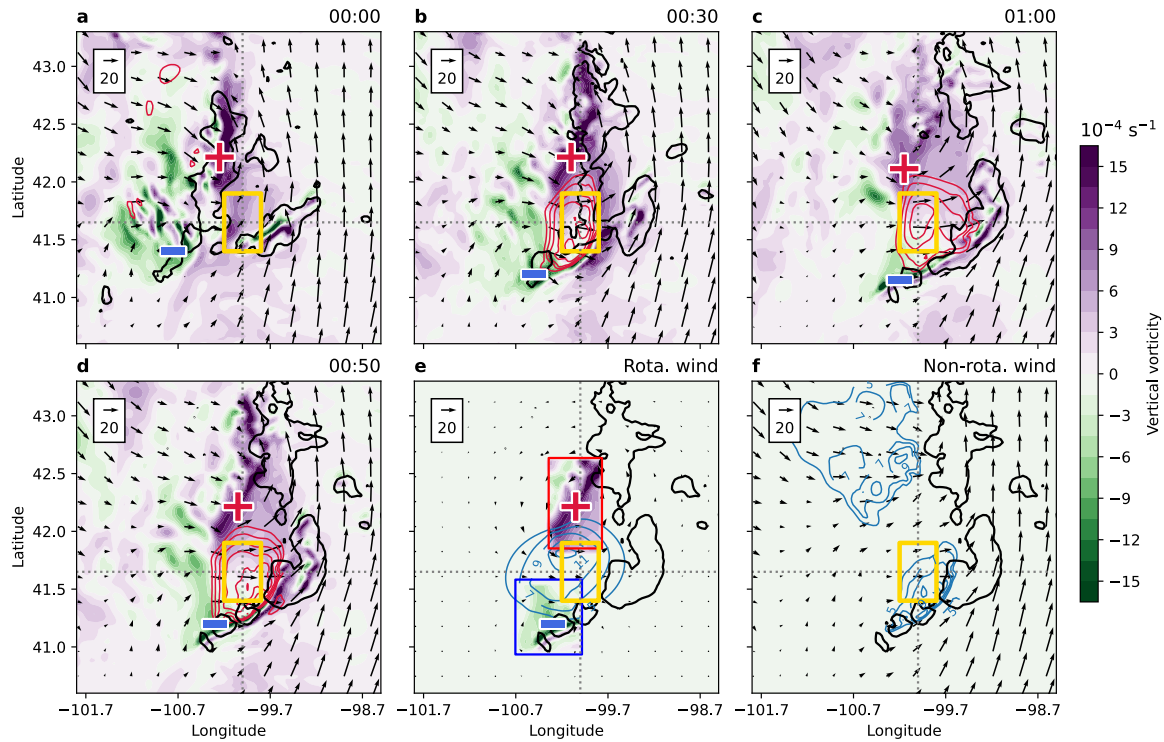


Figure 11. Horizontal distribution of vertical vorticity (shading, s^{-1}), wind vectors, and system-relative meridional winds (red contours, starting from $8 m s^{-1}$ at an interval of $2 m s^{-1}$) at 1.35 km above ground level, and maximum column radar reflectivity (black contours, 40 dBZ) at (a) 0000, (b) 0030, (c) 0100, and (d) 0050 LST on 24 May 2020. (e) Rotational component (wind vectors) derived from bookend vortices (shading, s^{-1}) and (f) non-rotational component (wind vectors) and maximum column radar reflectivity (black contours, 40 dBZ) at 0050 LST. Blue contours in (e, f) display wind speeds exceeding $5 m s^{-1}$. Yellow boxes indicate the region of the strongest rear inflow jet intensity at 0050 LST, used to plot Figure 12. Significant positive and negative vertical vorticity centers are marked by “+,” “−,” respectively.

$$\nabla^2\psi = \zeta = \frac{\partial v}{\partial y} - \frac{\partial u}{\partial x} \quad (3)$$

Then the rotational component (u_r, v_r) is obtained by horizontally differentiating the streamfunction, and the non-rotational component (u_n, v_n) is derived by subtracting the rotational wind from the full wind,

$$\begin{cases} u_r = -\frac{\partial\psi}{\partial y}, & u_n = u - u_r \\ v_r = \frac{\partial\psi}{\partial x}, & v_n = v - v_r \end{cases} \quad (4)$$

Figure 11e shows the rotational wind associated with the bookend vortices at 0050 LST when the RIJ is the strongest. It is observed that the bookend vortices accompany a westerly flow of approximately $11\text{--}13 m s^{-1}$ along the axis of the RIJ (Figure 11b), accounting for an average of 38.7% of the RIJ strength (Figure 12). Furthermore, the temporal variation in the contribution of these vortices remains consistent both before and during the merger, ranging from 30% to 50%. Additionally, despite a surge in RIJ strength during the merger, the proportion of the rotational wind decreases by approximately 10%, which can be attributed to the weakening of the vortices (Figure 11). These findings suggest that while the bookend vortices play a role in RIJ dynamics, they may not significantly accelerate the RIJ in this case.

4. Summary and Discussion

In the present study, the rapid update four-dimensional variational data assimilation system (VDRAS) was utilized to investigate the genesis of a bow echo following the squall line-supercell merger over the Great Plains of

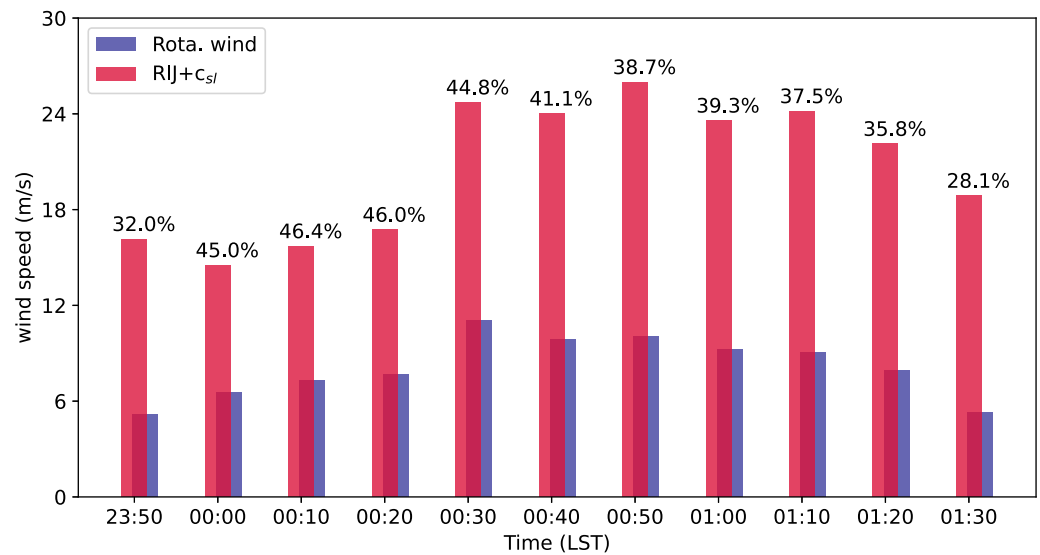


Figure 12. Temporal evolution of mean full wind speed ($RIJ + c_{sl}$) and its rotational component (Rota. wind) within the yellow box in Figure 11. The contribution of rotational wind (bookend vortices) to the full wind speed at each time is also labeled.

the United States on 23–24 May 2020. This merger occurred when an eastward-propagating squall line encountered a supercell ahead of it, resulting in the formation of a compact bow echo with an intense RIJ. While the impact of such merging processes on bow echo formation has been previously assessed via idealized simulations (FP14), our results based on observational data reveal both similarities and differences.

Consistent with FP14, the merger process began with a weakening of the squall line, primarily due to the blocking of its inflow by the supercell. However, unlike the locally strengthening cold pool and RIJ due to the merger observed in FP14, this case exhibited two distinct RIJs. A classic RIJ formed atop the cold pool on the northern side of the squall line and dissipated prior to the merger. During the merger, another RIJ emerged as low-level westerlies in the central squall line accelerated toward the supercell, generating the bow echo. Interestingly, it was shown that this RIJ established ahead of the squall line, and then spread forward within the gap between the two systems (Figure 13), distinguishing it significantly from the classic RIJ described by Weisman (1992) and many other studies.

During the merger, diagnostic analysis of the pressure field revealed that the acceleration of the low-level westerlies was primarily driven by the dynamic lowering of pressure within the supercell, specifically the mesolow (or mesocyclone) created by the rotating updraft. This updraft also significantly intensified prior to the merger, releasing latent heat and generating a deep-tropospheric ($n = 1$) gravity wave associated with near-surface westerlies, thereby enhancing the RIJ. As the merger progressed, the squall line's cold pool gradually weakened due to the lack of evaporative cooling. However, the substantial negative horizontal vorticity at its leading edge favored the forward expansion of the RIJ and aided in its descent to the ground. Further examination of the role of the bookend vortices suggests that their contribution to the RIJ remained 30%–50% throughout the process. Despite a dramatic enhancement in RIJ intensity during the merger, there was a $\sim 10\%$ reduction in the rotational component, indicating that the bookend vortices did not drive RIJ acceleration but rather evolved alongside it.

The transition of severe weather from primarily hails (produced by the supercell) before the merger to widespread damaging winds after bowing aligns well with the climatology study by French and Parker (2012) and the simulated results (FP14). Most of the high winds were observed near the arching bow echo, providing important insights for practical severe weather forecasting. Moreover, the timeline of this event highlights that such a merger could mark the transition of severe weather types (Figure 4), thus providing an early warning for the local community. Therefore, given that merger duration may vary in different cases, we suggest that a 30-min to 1-hr lead time could be available for issuing wind-related warnings when the two systems are about to merge.

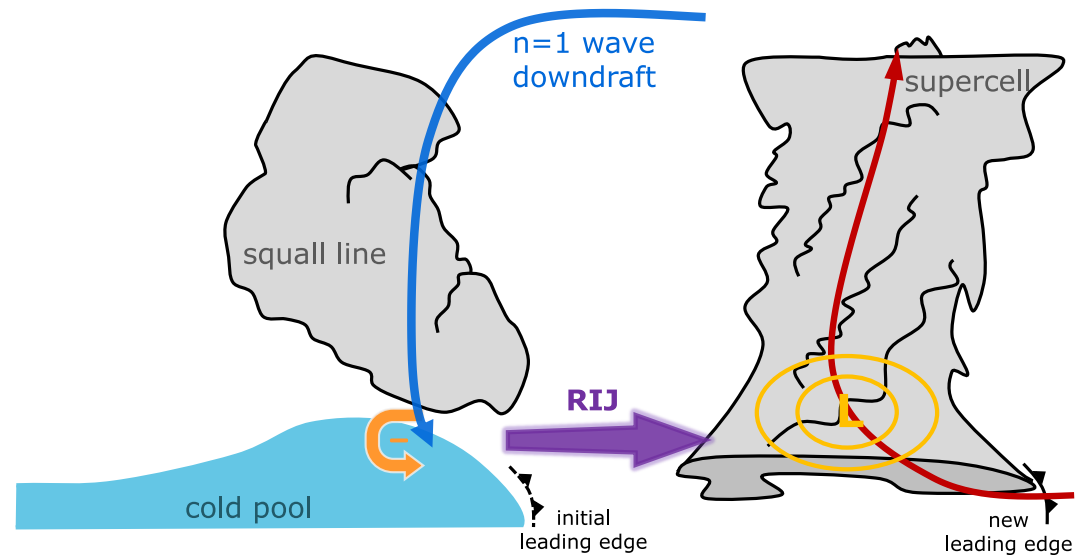


Figure 13. Conceptual diagram illustrating the formation of a rear inflow jet due to a squall line-supercell merger.

This study provides comprehensive insights into the system-scale processes leading to the genesis of a bow echo from a squall line-supercell merger. Our findings highlight that while idealized simulations are valuable for understanding the self-organization of convection, convective interactions in real-world scenarios are often more complex and intriguing. Furthermore, although our preliminary WRF run with 1-km horizontal grid-spacing failed to reproduce the system merger, a typical RIJ and a bow echo still formed in accordance with the classic theory. However, significant deviations in their locations and intensities compared to the observations suggest the substantial impact of such a merger on the forward-expanding RIJ. Future research could explore the sensitivity of supercell strength and location to variations in bow echo formation, based on observations, as examined by FP14 through idealized simulations. Studies in South China by Zhou et al. (2020, 2023) and Liu et al. (2023) have also demonstrated that bow echoes can form through the merger of squall lines with convective cells, revealing diverse governing mechanisms. With denser and more varied observations, as well as advanced tools like hybrid assimilation and artificial intelligence, we can expect to gain deeper insights into the diversity of convective activities and make improvements in nowcasting.

Data Availability Statement

The NCEP GFS analysis (<https://rda.ucar.edu/datasets/ds084-1/>) (NCEP/National Weather Service/NOAA/U.S. Department of Commerce, 2015) used to drive WRF, the ASOS data (https://mesonet.agron.iastate.edu/request/download.phtml?network=CO_ASOS) (NOAA National Centers for Environmental Information, 2021) and the Next Generation Weather Radar (NEXRAD) data (<https://aws.amazon.com/public-datasets/nexrad/>) (NOAA National Weather Service Radar Operations Center, 1991) assimilated into VDRAS are all publicly available.

References

- Atkins, N. T., Arnott, J. M., Przybylinski, R. W., Wolf, R. A., & Ketcham, B. D. (2004). Vortex structure and evolution within bow echoes. Part I: Single-Doppler and damage analysis of the 29 June 1998 derecho. *Monthly Weather Review*, 132(9), 2224–2242. [https://doi.org/10.1175/1520-0493\(2004\)132<2224:VSAEWB>2.0.CO;2](https://doi.org/10.1175/1520-0493(2004)132<2224:VSAEWB>2.0.CO;2)
- Burke, P. C., & Schultz, D. M. (2004). A 4-Yr climatology of cold-season bow echoes over the continental United States. *Weather and Forecasting*, 19(6), 1061–1074. <https://doi.org/10.1175/811.1>
- Chen, X., Zhao, K., Sun, J., Zhou, B., & Lee, W.-C. (2016). Assimilating surface observations in a four-dimensional variational Doppler radar data assimilation system to improve the analysis and forecast of a squall line case. *Advances in Atmospheric Sciences*, 33(10), 1106–1119. <https://doi.org/10.1007/s00376-016-5290-0>
- Davis, C., Atkins, N., Bartels, D., Bosart, L., Coniglio, M., Bryan, G., et al. (2004). The bow echo and MCV experiment: Observations and opportunities. *Bulletin of the American Meteorological Society*, 85(8), 1075–1094. <https://doi.org/10.1175/BAMS-85-8-1075>
- Du, Y., Rotunno, R., Chen, Z., & Yang, H. (2024). A linear theory for periodic convectively forced gravity waves near a coastline. *Journal of the Atmospheric Sciences*, 81(7), 1271–1288. <https://doi.org/10.1175/JAS-D-23-0173.1>

Acknowledgments

This study was supported by the National Natural Science Foundation of China (Grants 424B2033 and 42475002), the Guangdong Major Project of Basic and Applied Basic Research (Grants 2020B0301030004, 2024A1515510005, and 2025A1515011974), project supported by Southern Marine Science and Engineering Guangdong Laboratory (Zhuhai) (SML2024SP012, 311024001, and SML2024SP035), and the Key Innovation Team of the China Meteorological Administration (CMA2023ZD08). We also acknowledge the high-performance computing support from the School of Atmospheric Sciences of Sun Yat-sen University. The authors thank NCAR for supporting the first author's visit and for providing computing resources and VDRAS access during his stay. NCAR is sponsored by the National Science Foundation of the United States.

- Finley, C. A., Cotton, W. R., & Pielke, R. A. (2001). Numerical simulation of tornadogenesis in a high-precipitation supercell. Part I: Storm evolution and transition into a bow echo. *Journal of the Atmospheric Sciences*, 58(13), 1597–1629. [https://doi.org/10.1175/1520-0469\(2001\)058<1597:NSOTIA>2.0.CO;2](https://doi.org/10.1175/1520-0469(2001)058<1597:NSOTIA>2.0.CO;2)
- Forbes, G. S., & Wakimoto, R. M. (1983). A concentrated outbreak of tornadoes, downbursts and microbursts, and implications regarding vortex classification. *Monthly Weather Review*, 111(1), 220–236. [https://doi.org/10.1175/1520-0493\(1983\)111<0220:ACOOTD>2.0.CO;2](https://doi.org/10.1175/1520-0493(1983)111<0220:ACOOTD>2.0.CO;2)
- French, A. J., & Parker, M. D. (2012). Observations of mergers between squall lines and isolated supercell thunderstorms. *Weather and Forecasting*, 27(2), 255–278. <https://doi.org/10.1175/WAF-D-11-00058.1>
- French, A. J., & Parker, M. D. (2014). Numerical simulations of bow echo formation following a squall line–supercell merger. *Monthly Weather Review*, 142(12), 4791–4822. <https://doi.org/10.1175/MWR-D-13-00356.1>
- Fujita, T. T. (1978). *Manual of downburst prediction for Project NIMROD*. Department of Geophysical Sciences, University of Chicago.
- Fujita, T. T. (1979). Objective, operation, and results of Project NIMROD (pp. 259–266). Retrieved from <http://hdl.handle.net/10605/261973>
- Goodman, S. J., & Knupp, K. R. (1993). Tornadogenesis via squall line and supercell interaction: The November 15, 1989, Huntsville, Alabama, Tornado. In C. Church, D. Burgess, C. Doswell, & R. Davies-Jones (Eds.), *Geophysical monograph series* (Vol. 79, pp. 183–199). American Geophysical Union. <https://doi.org/10.1029/GM079p0183>
- Grim, J. A., Rauber, R. M., McFarquhar, G. M., Jewett, B. F., & Jorgensen, D. P. (2009). Development and forcing of the rear inflow jet in a rapidly developing and decaying squall line during BAMEX. *Monthly Weather Review*, 137(4), 1206–1229. <https://doi.org/10.1175/2008MWR2503.1>
- Jirak, I. L., Cotton, W. R., & McAnelly, R. L. (2003). Satellite and radar survey of mesoscale convective system development. *Monthly Weather Review*, 131(10), 2428–2449. [https://doi.org/10.1175/1520-0493\(2003\)131<2428:SARSOM>2.0.CO;2](https://doi.org/10.1175/1520-0493(2003)131<2428:SARSOM>2.0.CO;2)
- Jorgensen, D. P., & Smull, B. F. (1993). Mesovortex circulations seen by airborne Doppler radar within a bow-echo mesoscale convective system. *Bulletin of the American Meteorological Society*, 74(11), 2146–2157. [https://doi.org/10.1175/1520-0477\(1993\)074<2146:MCSBAD>2.0.CO;2](https://doi.org/10.1175/1520-0477(1993)074<2146:MCSBAD>2.0.CO;2)
- Klemp, J. B. (1987). Dynamics of tornadic thunderstorms. *Annual Review of Fluid Mechanics*, 19(1), 369–402. <https://doi.org/10.1146/annurev.fl.19.010187.002101>
- Klimowski, B. A., Hjeltnelt, M. R., & Bunkers, M. J. (2004). Radar observations of the early evolution of bow echoes. *Weather and Forecasting*, 19(4), 727–734. [https://doi.org/10.1175/1520-0434\(2004\)019<0727:ROOTEE>2.0.CO;2](https://doi.org/10.1175/1520-0434(2004)019<0727:ROOTEE>2.0.CO;2)
- Lafore, J.-P., & Moncrieff, M. W. (1989). A numerical investigation of the organization and interaction of the convective and stratiform regions of tropical squall lines. *Journal of the Atmospheric Sciences*, 46(4), 521–544. [https://doi.org/10.1175/1520-0469\(1989\)046<0521:ANIOTO>2.0.CO;2](https://doi.org/10.1175/1520-0469(1989)046<0521:ANIOTO>2.0.CO;2)
- Liu, Q., Xu, X., Zhao, K., & Zhou, A. (2023). A merger-formation bow echo caused by low-level mesovortex in South China. *Journal of Geophysical Research: Atmospheres*, 128(8), e2022JD037954. <https://doi.org/10.1029/2022JD037954>
- Moller, A. R., Doswell, C. A., Foster, M. P., & Woodall, G. R. (1994). The operational recognition of supercell thunderstorm environments and storm structures. *Weather and Forecasting*, 9(3), 327–347. [https://doi.org/10.1175/1520-0434\(1994\)009<0327:TOST>2.0.CO;2](https://doi.org/10.1175/1520-0434(1994)009<0327:TOST>2.0.CO;2)
- NCEP/National Weather Service/NOAA/U.S. Department of Commerce. (2015). NCEP GFS 0.25 degree global forecast grids historical archive [Dataset]. *Research Data Archive at the National Center for Atmospheric Research, Computational and Information Systems Laboratory*. <https://doi.org/10.5065/D65D8PWK>
- Nicholls, M. E., Pielke, R. A., & Cotton, W. R. (1991). Thermally forced gravity waves in an atmosphere at rest. *Journal of the Atmospheric Sciences*, 48(16), 1869–1884. [https://doi.org/10.1175/1520-0469\(1991\)048<1869:TFGWIA>2.0.CO;2](https://doi.org/10.1175/1520-0469(1991)048<1869:TFGWIA>2.0.CO;2)
- NOAA National Centers for Environmental Information. (2021). Automated surface/weather observing systems (ASOS/AWOS) [Dataset]. *National Oceanic and Atmospheric Administration*. Retrieved from <https://www.ncei.noaa.gov/products/land-based-station/automated-surface-weather-observing-systems>
- NOAA National Weather Service Radar Operations Center. (1991). NOAA next generation radar (NEXRAD) level 2 base data [Dataset]. *NOAA National Centers for Environmental Information*. <https://doi.org/10.7289/V5W9574V>
- Nolen, R. H. (1959). A radar pattern associated with tornadoes. *Bulletin of the American Meteorological Society*, 40(6), 277–279. <https://doi.org/10.1175/1520-0477-40.6.277>
- Przybylinski, R. W. (1995). The bow echo: Observations, numerical simulations, and severe weather detection methods. *Weather and Forecasting*, 10(2), 203–218. [https://doi.org/10.1175/1520-0434\(1995\)010<0203:TBEONS>2.0.CO;2](https://doi.org/10.1175/1520-0434(1995)010<0203:TBEONS>2.0.CO;2)
- Rotunno, R., & Klemp, J. (1985). On the rotation and propagation of simulated supercell thunderstorms. *Journal of the Atmospheric Sciences*, 42(3), 271–292. [https://doi.org/10.1175/1520-0469\(1985\)042<0271:OTRAPO>2.0.CO;2](https://doi.org/10.1175/1520-0469(1985)042<0271:OTRAPO>2.0.CO;2)
- Sieveking, J. E., & Przybylinski, R. W. (2004). The interaction of a high-precipitation supercell thunderstorm and bow echo to produce a prolonged severe wind event in east Central Missouri. 7A.5. Retrieved from <https://ams.confex.com/ams/11aram22sls/webprogram/Paper81818.html>
- Smull, B. F., & Houze, R. A. (1987). Rear inflow in squall lines with trailing stratiform precipitation. *Monthly Weather Review*, 115(12), 2869–2889. [https://doi.org/10.1175/1520-0493\(1987\)115<2869:RIISLW>2.0.CO;2](https://doi.org/10.1175/1520-0493(1987)115<2869:RIISLW>2.0.CO;2)
- Sun, J., Li, R., Zhang, Q., Trier, S. B., Ying, Z., & Xu, J. (2023). Mesoscale factors contributing to the extreme rainstorm on 20 July 2021 in Zhengzhou, China, as revealed by rapid update 4Dvar analysis. *Monthly Weather Review*, 151(8), 2153–2176. <https://doi.org/10.1175/MWR-D-22-0337.1>
- Trapp, R. J., & Weisman, M. L. (2003). Low-level mesovortices within squall lines and bow echoes. Part II: Their genesis and implications. *Monthly Weather Review*, 131(11), 2804–2823. [https://doi.org/10.1175/1520-0493\(2003\)131<2804:LMWSLA>2.0.CO;2](https://doi.org/10.1175/1520-0493(2003)131<2804:LMWSLA>2.0.CO;2)
- Wakimoto, R. M., Murphree, H. V., Davis, C. A., & Atkins, N. T. (2006). High winds generated by bow echoes. Part II: The relationship between the mesovortices and damaging straight-line winds. *Monthly Weather Review*, 134(10), 2813–2829. <https://doi.org/10.1175/MWR3216.1>
- Wakimoto, R. M., Murphree, H. V., Nester, A., Jorgensen, D. P., & Atkins, N. T. (2006). High winds generated by bow echoes. Part I: Overview of the Omaha bow echo 5 July 2003 storm during BAMEX. *Monthly Weather Review*, 134(10), 2793–2812. <https://doi.org/10.1175/MWR3215.1>
- Wakimoto, R. M., Stauffer, P., & Lee, W.-C. (2015). The vertical vorticity structure within a squall line observed during BAMEX: Banded vorticity features and the evolution of a bowing segment. *Monthly Weather Review*, 143(1), 341–362. <https://doi.org/10.1175/MWR-D-14-00246.1>
- Weisman, M. L. (1992). The role of convectively generated rear-inflow jets in the evolution of long-lived mesoconvective systems. *Journal of the Atmospheric Sciences*, 49(19), 1826–1847. [https://doi.org/10.1175/1520-0469\(1992\)049<1826:TROCGR>2.0.CO;2](https://doi.org/10.1175/1520-0469(1992)049<1826:TROCGR>2.0.CO;2)
- Weisman, M. L. (1993). The genesis of severe, long-lived bow echoes. *Journal of the Atmospheric Sciences*, 50(4), 645–670. [https://doi.org/10.1175/1520-0469\(1993\)050<0645:TGOSLL>2.0.CO;2](https://doi.org/10.1175/1520-0469(1993)050<0645:TGOSLL>2.0.CO;2)
- Weisman, M. L. (2001). Bow echoes: A tribute to T. T. Fujita. *Bulletin of the American Meteorological Society*, 82(1), 97–116. [https://doi.org/10.1175/1520-0477\(2001\)082<0097:BEATTT>2.3.CO;2](https://doi.org/10.1175/1520-0477(2001)082<0097:BEATTT>2.3.CO;2)

- Weisman, M. L., & Davis, C. A. (1998). Mechanisms for the generation of mesoscale vortices within quasi-linear convective systems. *Journal of the Atmospheric Sciences*, 55(16), 2603–2622. [https://doi.org/10.1175/1520-0469\(1998\)055<2603:MFTGOM>2.0.CO;2](https://doi.org/10.1175/1520-0469(1998)055<2603:MFTGOM>2.0.CO;2)
- Weisman, M. L., & Trapp, R. J. (2003). Low-level mesovortices within squall lines and bow echoes. Part I: Overview and dependence on environmental shear. *Monthly Weather Review*, 131(11), 2779–2803. [https://doi.org/10.1175/1520-0493\(2003\)131<2779:LMWSLA>2.0.CO;2](https://doi.org/10.1175/1520-0493(2003)131<2779:LMWSLA>2.0.CO;2)
- Wheatley, D. M., Trapp, R. J., & Atkins, N. T. (2006). Radar and damage analysis of severe bow echoes observed during BAMEX. *Monthly Weather Review*, 134(3), 791–806. <https://doi.org/10.1175/MWR3100.1>
- Wilhelmson, R. B., & Klemp, J. B. (1978). A numerical study of storm splitting that leads to long-lived storms. *Journal of the Atmospheric Sciences*, 35(10), 1974–1986. [https://doi.org/10.1175/1520-0469\(1978\)035<1974:ANSOSS>2.0.CO;2](https://doi.org/10.1175/1520-0469(1978)035<1974:ANSOSS>2.0.CO;2)
- Xu, X., Xue, M., & Wang, Y. (2015). Mesovortices within the 8 May 2009 bow echo over the central United States: Analyses of the characteristics and evolution based on Doppler radar observations and a high-resolution model simulation. *Monthly Weather Review*, 143(6), 2266–2290. <https://doi.org/10.1175/MWR-D-14-00234.1>
- Xu, X., Ju, Y., Liu, Q., Zhao, K., Xue, M., Zhang, S., et al. (2024). Dynamics of two episodes of high winds produced by an unusually long-lived quasi-linear convective system in South China. *Journal of the Atmospheric Sciences*, 81(8), 1449–1473. <https://doi.org/10.1175/jas-d-23-0047.1>
- Yang, H., & Du, Y. (2024). Difference between upshear- and downshear-propagating waves associated with the development of squall lines. *Monthly Weather Review*, 152(6), 1399–1420. <https://doi.org/10.1175/MWR-D-23-0109.1>
- Yang, H., Du, Y., & Sun, J. (2025). The merger of a supercell and squall line in the Great Plains. Part 1: Initiation of the supercell. *Journal of Geophysical Research: Atmospheres*, 130, e2024JD042393. <https://doi.org/10.1029/2024JD042393>
- Zhang, L., Sun, J., Ying, Z., & Xiao, X. (2021). Initiation and development of a squall line crossing Hangzhou Bay. *Journal of Geophysical Research: Atmospheres*, 126(1), e2020JD032504. <https://doi.org/10.1029/2020JD032504>
- Zhou, A., Zhao, K., Lee, W., Huang, H., Hu, D., & Fu, P. (2020). VDRAS and polarimetric radar investigation of a bow echo formation after a squall line merged with a preline convective cell. *Journal of Geophysical Research: Atmospheres*, 125(7), e2019JD031719. <https://doi.org/10.1029/2019JD031719>
- Zhou, A., Zhao, K., Xu, X., Liu, Q., Ding, Z., Huang, H., et al. (2023). A climatological study on the two types of bow echoes over South China. *Journal of Geophysical Research: Atmospheres*, 128(18), e2023JD038720. <https://doi.org/10.1029/2023JD038720>